Proceedings of the Pakistan Academy of Sciences: Part A
Physical and Computational Sciences 59(2): 47-60 (2022)

ISSN (Print): 2518-4245; ISSN (Online): 2518-4253
https://doi.org/10.53560/PPASA(59-2)760

Pakistan Academy of Sciences

Research Article

Design of Fractional Order Sliding Mode Adaptive Fuzzy Switching Controllers for Uncertain ACP1000 Nuclear Reactor Dynamics

Arshad H. Malik[1*], Aftab A. Memon[2], and Feroza Arshad[3]

[1]Department of Maintenance Training, Pakistan Atomic Energy Commission, A-104, Block-B, Kazimablad, Model Colony, Karachi, Pakistan
[2]Meritorious Professor and Ex-Chairman Department of Telecommunication Engineering, Mehran University of Engineering and Technology, Jamshoro, Sindh, Pakistan
[3]Department of Management Information System, Pakistan Atomic Energy Commission, B-63, Block-B, Kazimablad, Model Colony, Karachi, Pakistan

Abstract: Advanced Chinese Pressurized Water Reactor (ACP1000) is a third generation load following nuclear reactor. ACP1000 is designed to control the reactor power by a sophisticated control rod mechanism under the base load normal operation of a nuclear power plant in Mode-G. To extend the normal operation of ACP1000 for load following condition, boron adjustment control is used in manual configuration. In this research work, model based two new controllers are designed for ACP1000 reactor dynamics. A nonlinear two-point reactor kinetics model is developed for two halves of the reactor core designated as top and bottom of reactor core. Reactor feedbacks model for two-point reactor kinetics model is developed with fuel temperature, moderator temperature, Xenon concentration, G-Bank control rod position, R-Bank control rod position and boron concentration feedbacks under normal operation of ACP1000. Two problems of the large reactor core of ACP1000 are Xenon oscillations and axial offset in core power distribution. To address these problems, two new controllers are designed for normal load following operation of ACP1000. One controller is designed to replace G1-Bank and R-Bank in Mode-G for reactor power control. The second controller is designed to replace G2-Bank in Mode-G for reactivity control and axial power distribution control. Originally, both reactor coolant average temperature controller and reactor power controller were adaptive controllers. Therefore, both new controllers are designed based on an optimized sliding algorithm using a dedicated fractional order sliding mode control oriented adaptive fuzzy logic control (FO-SMC-AFLC) synthesis scheme. The performance of the proposed closed loop controllers is evaluated for design step and ramp power transients. Both proposed controllers are validated against benchmark results reported in Preliminary Safety Analysis Report (PSAR) of ACP1000. The novel control design scheme is proved satisfactory for normal load following operation of ACP1000, and all the results are found well within design limits.

Keywords: ACP1000, G and R-Banks, Reactor Dynamics, Fractional Order, Sliding Mode Control, Adaptive Fuzzy Logic

1. INTRODUCTION

In this research work, modeling and control design of Advanced Chinese Pressurized Water Reactor of 1100 MWe rating (ACP1000) based nuclear power plant is attempted.

The design and safety aspects of ACP1000 nuclear power plant are presented in [1-3]. The reactor dynamics and its original reactor power controller design aspects are covered in [4], while the controller design algorithm in mode-G under load following operation is presented in [5]. A research is conducted for adaptive fuzzy controller design for fractional order MIMO system with input saturation in [6]. A fractional order adaptive fuzzy controller is designed for uncertain robotic manipulators in [7]. An adaptive fuzzy sliding mode controller is designed for parallel manipulator with parametric uncertainties in [8]. An adaptive fuzzy

Received: August 2021; Accepted: June 2022
*Corresponding Author: Arshad H. Malik <mastermind_arshad@yahoo.com>

fractional sliding mode controller is synthesized for nonlinear multivariable system in [9]. A research work is explored in the direction of designing an adaptive fuzzy fractional sliding mode control for antilock braking system in [10]. An adaptive fractional order fuzzy sliding mode controller is made in designing the fractional order fuzzy sliding mode control for knee joint orthosis in [11]. An adaptive fractional order sliding mode fuzzy controller is designed for active power filter in [12]. The research is further extended with an adaptive back stepping fractional fuzzy sliding mode controller design for an active power filter in [13]. Robust fuzzy adaptive sliding mode controller is developed for fractional order chaos in [14]. A research is further extended for adaptive fuzzy fractional order sliding mode controller design for uncertain system in [15]. A two-point reactor kinetic model is developed for PWR and a load following axial offset LQG/LTR controller is designed in [16]. A fuzzy fractional PID controller is designed for PWR in [17]. Simulate-3K neutronic and thermal hydraulic modeling aspects are presented in [18].

In ACP1000 reactor dynamics, G-bank is designed for reactor power control and coolant temperature control, while R-bank is designed for reactor power control purposes. Two point reactor kinetics model (2PRKM) with feedbacks of G-bank and R-bank control rods (GR) and liquid poison as chemical shim dynamics (CSD) are integrated as 2PRKM-GR-CSD. In this research work, a two-point reactor kinetic model of ACP1000 with special emphasis on G-bank, R-bank and chemical shim dynamics (2PRKM-GR-CSD) is modelled for the first time, and a novel optimized fractional order sliding adaptive fuzzy logic algorithm is developed for reactivity control, axial power distribution control and hence reactor power control. The proposed control design structure for 2PRKM-GR-CSD is a Fractional Order Sliding Mode Control Adaptive Fuzzy Logic Controller (FO-SMC-AFLC).

2. MATERIALS AND METHODS

2.1 ACP1000 Reactor Dynamics

The reactor core of ACP1000 is large and therefore is modelled with two-point reactor kinetics (2PRKM) models. Top half reactor core is modelled by one PRKM and bottom half core is modelled by second PRKM. Neutron and precursor dynamics are represented by PRKM with six precursor groups. Since there are two PRKM, so both models are strongly coupled. Internal reactor dynamics is covered with fuel temperature dynamics (FTD), moderator temperature dynamics (MTD) and Xenon concentration dynamics (XCD), while external reactor dynamics is covered with control rod dynamics (CRD) and boron concentration dynamics (BCD). In ACP1000, Mode-G is used for temperature and reactor power control using G-bank and R-bank known as GR dynamics (GRD). G-bank consists of sub G1-bank and sub G2-bank while R-bank is a single bank. G-bank has more worth than R-bank because it is meant for temperature control and reactor power control, while R-bank is meant for power control only. Control rods are configured in Rod Control Cluster Assembly (RCCA) in a reactor core. The boron concentration dynamics is known as Chemical Shim Dynamics (CSD). The entire behaviour of 2PRKM, FTD, MTD, XCD, GRD and CSD is known as reactor dynamics of ACP1000. Axial offset is a more severe control problem than Xenon Oscillations because it covers the control rod dynamics with more reactivity worth.

2.2 Two-Point Reactor Kinetics Model of ACP1000

The top half reactor core is modelled by the top point reactor kinetic model for relative neutron power (Prt) as [16]:

$$\frac{dP_{rt}(t)}{dt} = \frac{\rho_t(t)-\beta}{\Lambda_t} P_{rt}(t) + \sum_{i=1}^{6} \lambda_i C_i(t) - P_{rbt}(t) \quad (1)$$

$$\frac{dC_{ti}(t)}{dt} = \frac{\beta_i}{\Lambda_t} P_{rt}(t) - \lambda_i C_{ti}(t) \quad (2)$$

Where the symbols have their usual meanings.

The bottom half reactor core is modelled by bottom point reactor kinetic model for relative neutron power (P_{rb}) as:

$$\frac{dP_{rb}(t)}{dt} = \frac{\rho_b(t)-\beta}{\Lambda_b} P_{rb}(t) + \sum_{i=1}^{6} \lambda_i C_i(t) - P_{rtb}(t) \quad (3)$$

$$\frac{dC_{bi}(t)}{dt} = \frac{\beta_i}{\Lambda_b} P_{rb}(t) - \lambda_i C_{bi}(t) \quad (4)$$

Where the symbols have their usual meanings.

The reactor core total relative power is given as:

$$P_r(t) = P_{rt}(t) + P_{rb}(t)$$

P_{rtb} and P_{rbt} are computed through a coupling coefficient as:

$$P_{rtb}(t) = \alpha(P_{rt}(t) - \frac{P_{b0}}{P_{to}} P_{rb}(t)) \quad (5)$$

$$P_{rbt}(t) = \alpha(P_{rb}(t) - \frac{P_{t0}}{P_{bo}} P_{rt}(t)) \quad (6)$$

Where α is the coupling coefficient.

The thermal hydraulics model is composed of FTD and MTD.

The top fuel temperature dynamics are given as:

$$\frac{dT_{ft}(t)}{dt} = \frac{P_{rt}(t)}{M_{ft}C_f} - \frac{(T_{ft}(t) - T_{ct}(t))}{R} \quad (7)$$

$$\frac{dT_{ct}(t)}{dt} = \frac{(T_{ft}(t) - T_{ct}(t))}{RM_{ct}C_{Pc}} - 2W_{ct}C_{pc}(T_{ct}(t) - T_{\text{int}}(t)) \quad (8)$$

The bottom fuel temperature dynamics is given as:

$$\frac{dT_{fb}(t)}{dt} = \frac{P_{rb}(t)}{M_{fb}C_f} - \frac{(T_{fb}(t) - T_{cb}(t))}{R} \quad (9)$$

$$\frac{dT_{cb}(t)}{dt} = \frac{(T_{fb}(t) - T_{cb}(t))}{RM_{cb}C_{Pc}} - 2W_{cb}C_{pc}(T_{cb} - T_{inb}) \quad (10)$$

The decay heat is used to calculate fuel and moderator temperatures. Therefore, 4th order coupled decay heat model is developed.

Where the symbols having their usual meanings.

The top Iodine concentration dynamics are given as:

$$\frac{dI_t(t)}{dt} = Y_{It}P_{rt}(t) - \lambda_{It}I_t(t) \quad (11)$$

The top Xenon concentration dynamics are given as:

$$\frac{dX_t(t)}{dt} = (3.12\times10^{10})\frac{Y_{Xt}}{V_t\Sigma_f}P_{rt}(t) - \lambda_{Xt}X_t(t) + \lambda_{It}X_t(t) - \sigma_X X_t(t)P_{rt}(t) \quad (12)$$

The bottom Iodine concentration dynamics is given as:

$$\frac{dI_b(t)}{dt} = Y_{Ib}P_{rb}(t) - \lambda_{Ib}I_b(t) \quad (13)$$

The bottom Xenon concentration dynamics is given as:

$$\frac{dX_b(t)}{dt} = (3.12\times10^{10})\frac{Y_{Xb}}{V_b\Sigma_f}P_{rb}(t) - \lambda_{Xb}X_b(t) + \lambda_{Ib}X_b(t) - \sigma_X X_b(t)P_{rb}(t) \quad (14)$$

Where the symbols having their usual meanings.
The top control rod G1-bank and R-bank reactivity is given as:

$$\frac{d\rho_{crt}(t)}{dt} = G_t r_t(t) + G_b r_b(t) \quad (15)$$

Where

$$G_t = f_t(G_{G1}^{PartLength}, G_{G2}^{PartLength}, G_R^{PartLength}) \quad (16)$$

$$r_t(t) = g_t(r_{G1}^{PartLength}(t), r_{G2}^{PartLength}(t), r_R^{PartLength}(t)) \quad (17)$$

$$G_b = f_b(G_{G1}^{FullLength}, G_{G2}^{FullLength}, G_R^{FullLength}) \quad (18)$$

$$r_b(t) = g_b(r_{G1}^{FullLength}(t), r_{G2}^{FullLength}(t), r_R^{FullLength}(t)) \quad (19)$$

The bottom control rod G1-bank and R-bank reactivity is given as:

$$\frac{d\rho_{crb}(t)}{dt} = G_b r_b(t) \quad (20)$$

The boron reactivity is given as:

$$\frac{d\rho_b(t)}{dt} = \Psi_b(\kappa_b, V, \Sigma_f, \sigma_b, N_W)b(t)P_r(t) \quad (21)$$

Where the symbols have their usual meanings.

2.3 ACP1000 Reactivity Feedbacks Model

The top reactivity is given as:

The top reactivity is given as:

$$\rho_t(t) = \alpha_f(T_{ft}(t) - T_{ft0}) + \alpha_c(T_{ct}(t) - T_{ct0}) - \rho_b(t) + \rho_{crt}(t) - \frac{\sigma_{aX}}{\nu\Sigma_f}(X_t(t) - X_{t0}) \quad (23)$$

The bottom reactivity is given as:

$$\rho_b(t) = \alpha_f(T_{fb}(t) - T_{fb0}) + \alpha_c(T_{cb}(t) - T_{cb0}) - \rho_b(t) + \rho_{crb}(t) - \frac{\sigma_{aX}}{\nu\Sigma_f}(X_b(t) - X_{b0}) \quad (24)$$

$$\rho_{cr}(t) = \rho_{crt}(t) + \rho_{crb}(t)$$

Where the symbols have their usual meanings.

2.4 State-Space Model Development of ACP1000 Reactor Dynamics

Nonlinear equations (1) to (4), equations (7) to (15) and equations (20) to (22) are linearized by a small perturbation method using the following equation:

$$x(t) = x_0 + \delta x(t)$$

The framework of the linearized ACP1000 reactor core model is shown in Fig. 1.

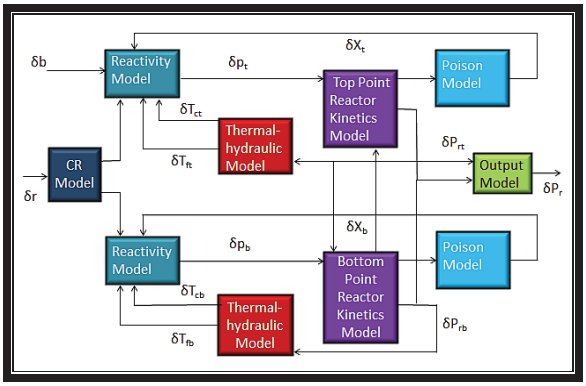

Fig. 1. Framework for Linearized ACP1000 reactor core model.

The linearized 26th order Multi-Input Multi-Output (MIMO) model is represented in state space form as:

$$\dot{x}(t) = A_{m\times m}x_{m\times 1}(t) + B_{m\times n}u_{n\times 1}(t) \quad (25)$$

$$y(t) = C_{p\times m}x_{m\times 1}(t) \quad (26)$$

Where u(t) and y(t) are the input and output vectors and defined as:

$$u(t) = [r_t \;\; r_b \;\; b]^T$$

$$y(t) = [P_{rt} \;\; P_{rb}]^T$$

Now the 26th order linearized MIMO model is decoupled into six SISO models using the transfer matrix in frequency domain as:

$$G(s) = \frac{Y(s)}{U(s)}$$

$$\begin{bmatrix} Y_1(s) \\ Y_2(s) \end{bmatrix} = \begin{bmatrix} G_{11}(s) & G_{12}(s) & G_{13}(s) \\ G_{21}(s) & G_{22}(s) & G_{23}(s) \end{bmatrix} \begin{bmatrix} U_1(s) \\ U_2(s) \\ U_3(s) \end{bmatrix} \quad (27)$$

Of six SISO sub-systems, four are of prime concern.

2.5 Parametric Uncertainties in ACP1000 Reactor Dynamics

The neutronic parametric uncertainties of ACP1000 reactor dynamics is accessed by using SIMULATE-3, which is an advanced transient nodal coupled neutronic thermal-hydraulic code, and the following parameters are found best estimated values with nominal values and parametric uncertainties:

$$\bar{\alpha}_f = \alpha_f \pm \Delta\alpha_f$$

$$\bar{\alpha}_c = \alpha_c \pm \Delta\alpha_c$$

$$\bar{\rho}_{G1} = \rho_{G1} \pm \Delta\rho_{G1}$$

$$\bar{\rho}_{G2} = \rho_{G2} \pm \Delta\rho_{G2}$$

$$\bar{\rho}_R = \rho_R \pm \Delta\rho_R$$

$$\bar{b} = b \pm \Delta b$$

Now equations (25) and (26) are revised as:

$$\dot{\bar{x}}(t) = (A + \Delta A)\bar{x}(t) + (B + \Delta B)u(t) \quad (27)$$

$$y(t) = (C + \Delta C)\bar{x}(t) \quad (28)$$

Equations (27) and (28) are rewritten as:

$$\dot{\bar{x}}(t) = \overline{A}\bar{x}(t) + \overline{B}u(t) \quad (29)$$

$$y(t) = \overline{C}\bar{x}(t) \quad (30)$$

2.5 FO-SMC-AFLC Controller Synthesis

2.5.1 Framework of FO-SMC-AFLC

Since in the original design, both reactor coolant average temperature controller and reactor power controller are adaptive in nature. Therefore, both new controllers are synthesized using an optimized sliding algorithm which mimics novel hybrid fractional order sliding surface and adaptive fuzzy scheme. Hence, it is the best novel design approach for the replacement of existing controllers with state-of-the-art novel controllers. The basic structure of the hybrid Fractional Order (FO), Sliding Mode Control (SMC) and Adaptive Fuzzy Logic Controller (AFLC) is shown in Fig. 2.

The inputs, outputs and interface of each FO, SMC and AFLC are very much obvious in Fig. 2. The concept of adaptation is also shown along with AFLC. This basic concept is adopted for the synthesis of two main and four sub-controllers.

2.5.2 Closed Loop Configuration of FO-SMC-AFLC Controller for ACP1000 Reactor Dynamics

Based on the framework of FO-SMC-AFLC presented in Fig. 2, the two advanced controllers are designed for reactor power control using G1-bank and R-bank designated as (FO-SMC-AFLC-1) and reactor power control using G2-bank, reactivity control and axial power distribution control designated as FO-SMC-AFLC-2 respectively. FO-SMC-AFLC-1 is further divided into two sub-controllers for control rod reactivity control designated as FO-SMC-AFLCr1) and boron reactivity control designated as FO-SMC-AFLCb1 respectively. Similarly, FO-SMC-AFLC-2 is

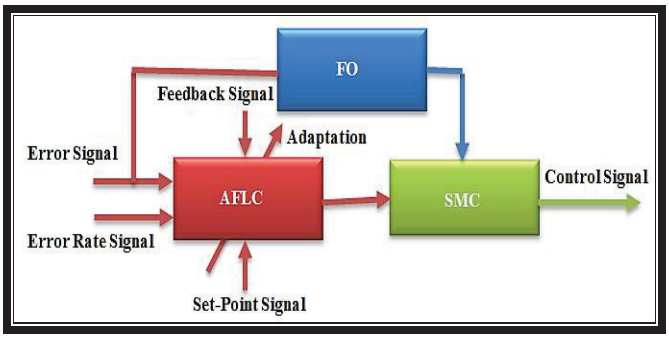

Fig. 2. Internal framework of FO-SMC-AFLC.

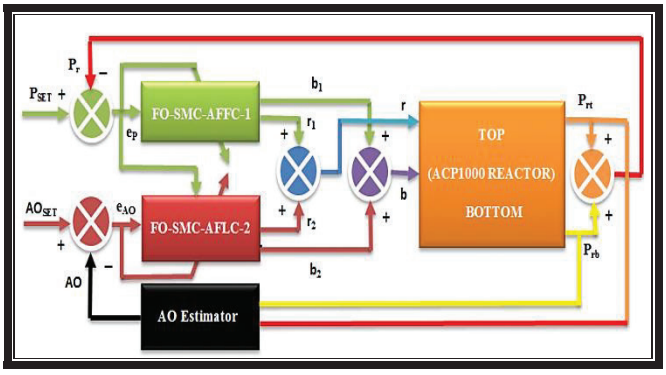

Fig. 3. Closed loop configuration of fractional order sliding mode adaptive fuzzy logic switching controllers for ACP1000 reactor dynamics.

further divided into two sub-controllers for control rod reactivity control designated as FO-SMC-AFLCr2 and boron reactivity control designated as FO-SMC-AFLCb2. The closed loop configuration of fractional order sliding mode adaptive fuzzy logic switching controllers for ACP1000 reactor dynamics is shown in Fig. 3.

The output of FO-SMC-AFLC-1 and FO-SMC-AFLC-2 are given as:

$$r(t) = r_1(t) + r_2(t) \tag{31}$$

$$b(t) = b_1(t) + b_2(t) \tag{32}$$

The output of AO estimator is given as:

$$AO(t) = \frac{P_{rt}(t) - P_{bt}(t)}{P_{rt}(t) + P_{bt}(t)} \tag{33}$$

The error signals for FO-SMC-AFLC-1 and FO-SMC-AFLC-2 are given as:

$$e_P(t) = P_{SET}(t) - P_r(t) \tag{34}$$

$$e_{AO}(t) = AO_{SET}(t) - AO(t) \tag{35}$$

The error rate signals for FO-SMC-AFLC-1 and FO-SMC-AFLC-2 are given as:

$$\dot{e}_P(t) = \frac{d(P_{SET}(t) - P_r(t))}{dt} \tag{36}$$

$$\dot{e}_{AO}(t) = \frac{d(AO_{SET}(t) - AO(t))}{dt} \tag{37}$$

Now, the outputs of two sub-controllers FO-SMC-AFLCr$_1$ and FO-SMC-AFLCb$_1$ are given as:

$$r_1(t) = \Psi_{r_1}(e_P(t), \dot{e}_P(t), FO_{r_1}, SMC_{r_1}, AFLC_{r_1}) \tag{38}$$

$$b_1(t) = \Psi_{b_1}(e_P(t), \dot{e}_P(t), FO_{b_1}, SMC_{b_1}, AFLC_{b_1}) \tag{39}$$

Now, the outputs of two sub-controllers FO-SMC-AFLCr$_2$ and FO-SMC-AFLCb$_2$ are given as:

$$r_2(t) = \Psi_{r_2}(e_P(t), e_{AO}(t), \dot{e}_P(t), \dot{e}_{AO}(t) FO_{r_2}, SMC_{r_2}, AFLC_{r_2}) \tag{40}$$

$$b_2(t) = \Psi_{b_2}(e_P(t), e_{AO}(t), \dot{e}_P(t), \dot{e}_{AO}(t) FO_{b_2}, SMC_{b_2}, AFLC_{b_2}) \tag{41}$$

Now, based on equation (29), equation (27) is redefined in time domain as a function of and t. State space model of top relative reactor power to top control rod reactivity is given as:

$$\dot{\bar{x}}(t) = f_{11}(\bar{x}, t) + \overline{B}_{f_{11}} u_1(t) \tag{42}$$

$$y_1(t) = \overline{C}_{f_{11}} \bar{x}(t) \tag{43}$$

State space model of top relative reactor power to boron reactivity is given as:

$$\dot{\bar{x}}(t) = f_{13}(\bar{x}, t) + \overline{B}_{f_{13}} u_3(t) \tag{44}$$

$$y_1(t) = \overline{C}_{f_{13}} \bar{x}(t) \tag{45}$$

State space model of bottom relative reactor power to bottom control rod reactivity is given as:

$$\dot{\bar{x}}(t) = f_{22}(\bar{x}, t) + \overline{B}_{f_{22}} u_2(t) \tag{46}$$

$$y_2(t) = \overline{C}_{f_{22}} \bar{x}(t) \tag{47}$$

State space model of bottom relative reactor power to boron reactivity is given as:

$$\dot{\bar{x}}(t) = f_{23}(\bar{x}, t) + \overline{B}_{f_{23}} u_3(t) \tag{48}$$

$$y_2(t) = \overline{C}_{f_{23}} \bar{x}(t) \tag{49}$$

Now sliding mode controller is structured for FO-SMC-AFLCr$_1$, FO-SMC-AFLCb$_1$, FO-SMC-AFLCr$_2$ and FO-SMC-AFLCb$_2$.

If η_l is the fractional order of derivative function $D^{\eta}{}_l$ then fractional order sliding mode controllers for all four sub-controllers are defined and modelled as [15]:

$$u_{11}(t) = u^F_{eq_{11}}(t) + K_{SMC_{11}}(D^{\eta}{}_1 e_p(t) + k_{11} e_p(t)) \tag{50}$$

Where k_{11} is the design parameter of function f11(.) and computed as:

$$\phi(r_1(x_{Position})) = k_{11} x_{Position} \tag{51}$$

$$\frac{d\phi(r_1(x_{Position}))}{dx_{Position}} = k_{11} \tag{52}$$

KSMC11 is the design gain and given as:

$$K_{SMC_{11}} = (k_{11} B_{f_{11}})^{-1} T \tag{53}$$

Where T is the positive definite matrix.

The equivalent controller with filter is given as:

$$u_{eq_{11}}^{F}(t)=\frac{1}{1+\tau_{F_{11}}s}u_{eq_{11}}(t) \tag{54}$$

Where τ_{F11} is the filter for high frequency components in control signal and s is the sliding surface defined as:

$$s=\{r_1:\theta(\bar{x},t)=0\}$$

Where $\theta(\bar{x},t)\approx\theta(x,t)$ is the sliding function and computed as:

$$\theta(\bar{x},t)=k_{11}(P_{SET}-r_1)=\Psi_\theta(\phi(x),\varphi(t))$$

The equivalent controller without filter is given as:

$$u_{eq_{11}}(t)=\frac{1}{k_{11}}\frac{d\varphi(t)}{dt}-f_{11}(\bar{x},t)$$

Similarly, rest of three FO-SMC for $f_{13}(.), f_{22}(.)$ and $f_{23}(.)$ are modeled as:

$$u_{13}(t)=u_{eq_{13}}(t)+K_{SMC_{13}}(D^{\eta_2}e_p(t)+k_{13}e_p(t)) \tag{55}$$

$$u_{22}(t)=u_{eq_{22}}(t)+K_{SMC_{22}}(D^{\eta_3}e_{AO}(t)+k_{22}e_p(t)) \tag{56}$$

$$u_{23}(t)=u_{eq_{23}}(t)+K_{SMC_{23}}(D^{\eta_4}e_{AO}(t)+k_{23}e_p(t)) \tag{57}$$

Now, the adaptive fuzzy logic controllers are structured based on the closed loop FO-SMC driven outputs, generated from ACP1000 reactor dynamics as outputs P_{rt}(t) and P_{rb} (t) respectively and one extracted signal as AO (t).

If $r_1(k)$ is LV^j , where LV^j is the j-th linguistic variable with j-th membership function (j) then j-th rule (R_j) is computed at k-th instant as:

$$R_j(k)=K_{IN11_j}P_{SET}(k)+K_{OUT11_j}r_1(k) \tag{58}$$

Where K_{IN1Ij} and K_{OUTIIj} are the input and output gains and are computed as:

$$K_{IN11_j}=\frac{a_j-0.1}{b_j} \tag{59}$$

$$K_{OUT11_j}=\frac{0.1-a_j+b_jK_{IN11_j}}{b_j}$$

Where aj and bj are the design scalar parameters of j-th membership function.

Now, the output of j-th adaptive fuzzy logic controller is given as:

$$u_{AFLC11}(k)=a_jR_j(k)+b_j(K_{IN11_j}P_{SET}(k)-K_{OUT11_j}r_1(k)) \tag{59}$$

Now, the value of k11 is rewritten as:

$$k_{11}=u_{AFLC11}(k) \tag{60}$$

The final control law is computed by substituting the value of k11 from equation (60) into equation (50) as:

$$u_{11}(t)=u_{eq_{11}}^{F}(t)+K_{SMC_{11}}(D^{\eta_1}e_p(t)+u_{AFLC11}e_p(t)) \tag{61}$$

Similarly, equations (53), (54) and (55) are updated as:

$$u_{13}(t)=u_{eq_{13}}^{F}(t)+K_{SMC_{13}}(D^{\eta_2}e_p(t)+u_{AFLC13}e_p(t)) \tag{62}$$

$$u_{22}(t)=u_{eq_{22}}^{F}(t)+K_{SMC_{22}}(D^{\eta_3}e_{AO}(t)+u_{AFLC22}e_p(t)) \tag{63}$$

$$u_{23}(t)=u_{eq_{23}}^{F}(t)+K_{SMC_{23}}(D^{\eta_4}e_{AO}(t)+u_{AFLC23}e_p(t)) \tag{64}$$

Now, equations (32) and (33) are rewritten as:

$$r(t)=r_1(t)+r_2(t)=u_{11}(t)+u_{13}(t) \tag{65}$$

$$b(t)=b_1(t)+b_2(t)=u_{22}(t)+u_{23}(t) \tag{66}$$

3. RESULTS AND DISCUSSIONS

EThere are six SISO sub-systems of 2PRKM-GR-CSD model. The behaviour of open loop and closed loop systems are evaluated in the following sections. All the modelling, design, simulation and analysis are carried out in a MATLAB environment.

3.1 Evaluation of 2PRKM-GR-CSD Model in Open Loop

The design parameters of open loop model are computed and optimized using a SIMULATE-3 neutronic and thermal-hydraulic code [18] which are tabulated for uncertain 2PRKM-GR-SCD model shown in Table 1.

Table 1. Optimized parameters of 2PRKM-GR-SCD

Design Parameters	Design Values
α	0.5
$\Delta\alpha_F$ (pcm/K)	±3.5
$\Delta\alpha_C$ (pcm/K)	±3.3
$\Delta\alpha_{G1}$ (pcm)	±42.5
$\Delta\alpha_{G2}$ (pcm)	±78.2
$\Delta\alpha_R$ (pcm)	±105.4
Δb (ppm)	±48
$m \times m$	26×26
$m \times n$	26×3
$p \times m$	2×26

In this research work, the pole-zero map of the model from top relative power to top control rod reactivity represented by equations (42) and (43) is shown in Fig. 4.

The presence of poles and zeros in the right half of S-plane shown in Fig. 4 proves that the sub-system is unstable. The open loop unit step response of this sub-system is shown in Fig. 5.

The open loop response shown in Fig. 5 clearly shows that the dynamics of the sub-system is unstable.

Similarly, the open loop response of other three sub-systems of interest is investigated and found unstable. The unstable dynamics is made stable through proper designing of sub-controllers.

3.2 Evaluation of FO-SMC-AFLC in Closed Loop

The closed loop evaluation of FO-SMC-AFLC-1 and FO-SMC-AFLC-2 is performed in Simulink. All the equations (1) through (66) are programmed and shown in the simulation model in Fig. 6.

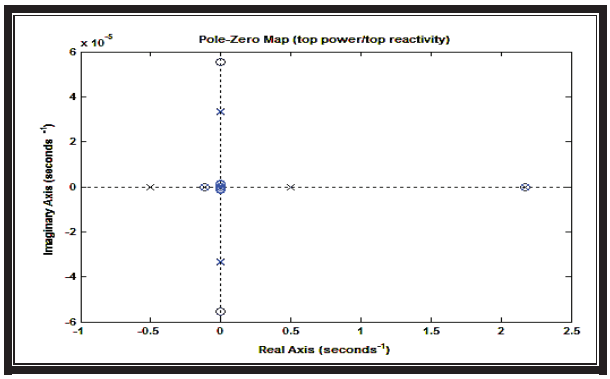

Fig. 4. Pole-Zero map of model from top relative power to top control rod reactivity.

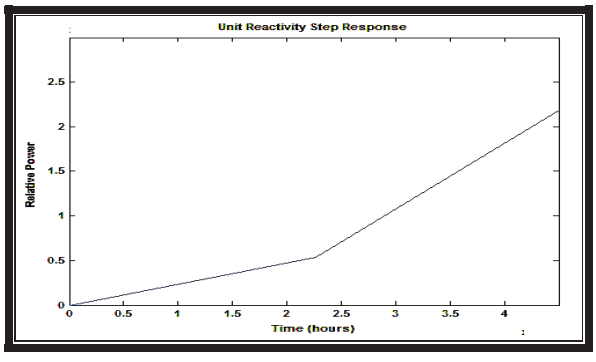

Fig. 5. Open loop unit step response of model from top relative power to top control rod reactivity.

The dynamic simulation is performed and assessed using two types of transient simulations. One is ramp transient, and the second is step transient simulation experiments.

The benchmark is the Preliminary Safety Analysis Report (PSAR) containing the results of the original reactor power control system with G-bank and R-bank. The redesigned proposed reactor power control system is designated as FO-SMC-AFLC.

The controller design constraints [4] are tabulated in Table 2.

The optimized design parameters of FO-SMC-AFLC-1 and FO-SMC-AFLC-2 are tabulated in Table 3.

3.2..1 Ramp Transient Simulations

In ramp power transient, the reactor power is increased from 40% to 50% at a rate of 5%/hr and then the reactor power is decreased from 50% to 30% at rate of 10%/hr. This ramp-up and ramp-down power sequence is followed in the transient analysis as per load following the procedure laid down in the design. The behaviour of FO-SMC-AFLC based closed loop system is shown in Fig. 7 against the desired ramp reference signal.

Table 2. Controller design constraints

Parameters	Value
Maximum Overshoot (%)	13
Settling Time (Sec)	900
AO band	$\pm$0.05
Step Power change rate (%)	10
Ramp Power change rate (%/min)	5

Table 3. Design parameters of FO-SMC-AFLC-1 and FO-SMC-AFLC-2

Design Parameters	Design Values
η_1	0.72
η_2	0.78
η_3	0.83
η_4	0.86
K_{SMC11}	1.8
K_{SMC13}	2.2
K_{SMC22}	4.3
K_{SMC23}	5.2
Value of j for FO-SMC-AFLCr_1	15
Value of j for FO-SMC-AFLCb_1	13
Value of j for FO-SMC-AFLCr_2	9
Value of j for FO-SMC-AFLCb_2	7
Scalar design parameters of FO-SMC-AFLC1	28
Scalar design parameters of FO-SMC-AFLC2	16

It is very much obvious from Fig. 7 that the relative reactor power tracks well the target ramp reactor power.

The performance of proposed control system for top and bottom halves of reactor core for ramp transient is shown in Fig. 8 and Fig. 9, respectively.

It is very much obvious from Fig. 7 that the relative reactor power tracks well the target ramp reactor power.

Top control rod reactivity with full and part length control rods, is computed and compared with benchmark results [1]. At the start of transient, when power is increased, the control rods are withdrawn due to which its reactivity becomes less negative. At constant power level, it remains almost constant. At the end of transient, when power is decreased from 50 % to 30%, the reactivity again becomes more negative.

Similar behaviour is observed for bottom control rod reactivity with only full length control rods in Fig. 9 and is computed and compared with benchmark results [1]. It includes full length control rods due to which the effect of reactivity is less as compared to top reactivity with the power manoeuvrings.

The performance of the proposed controller in terms of overshoot and settling time for ramp power changes are well within the designed constraints.
The variation of axial offset is shown in Fig. 10.

The performance of the proposed controller in terms of AO band for ramp power changes is well within the designed target band of □0.05.
The variation of boron concentration is shown in Fig. 11.

The output of second controller FO-SMC-AFLC-2 is the boron concentration which is computed

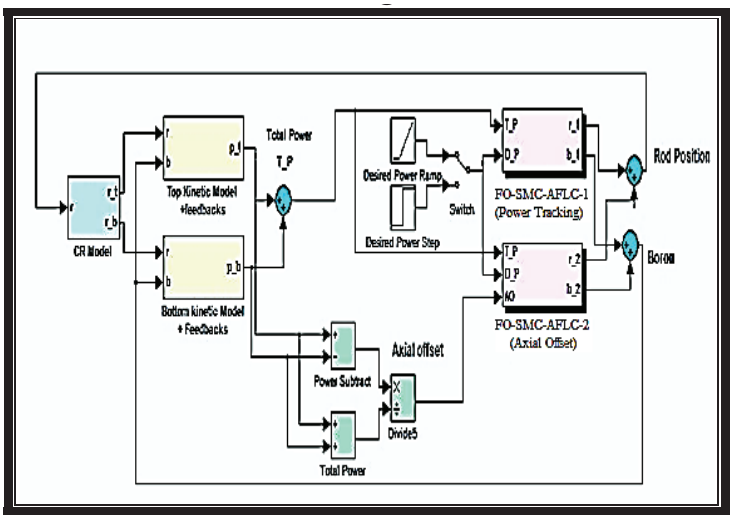

Fig. 6. Reactor power control redesign logic with two PRKM and AO for ACP1000.

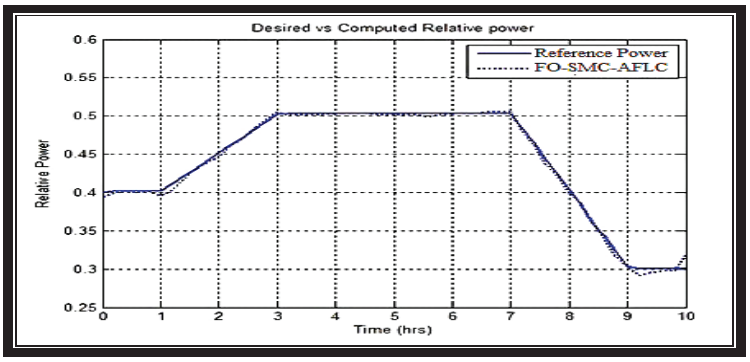

Fig. 7. Comparison of FO-SMC-AFLC and reference reactor powers under ramp power changes.

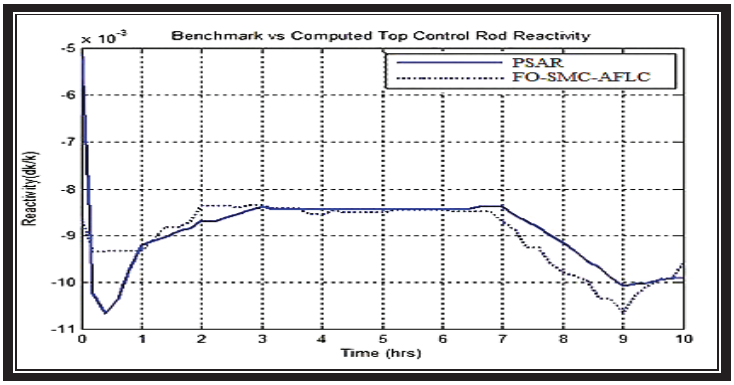

Fig. 8. Performance comparison of top control rod reactivity for ramp power changes.

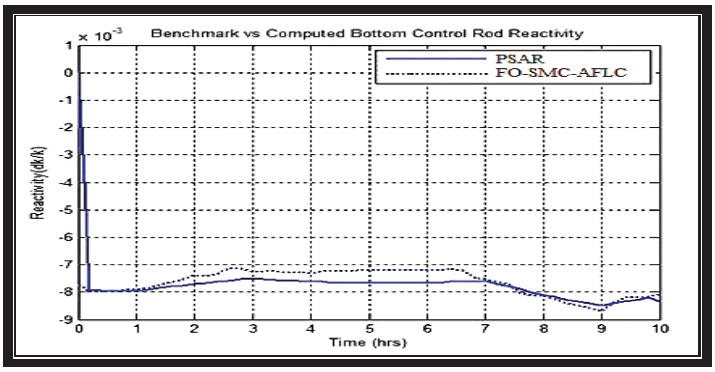

Fig. 9. Performance comparison of bottom control rod reactivity for ramp power changes.

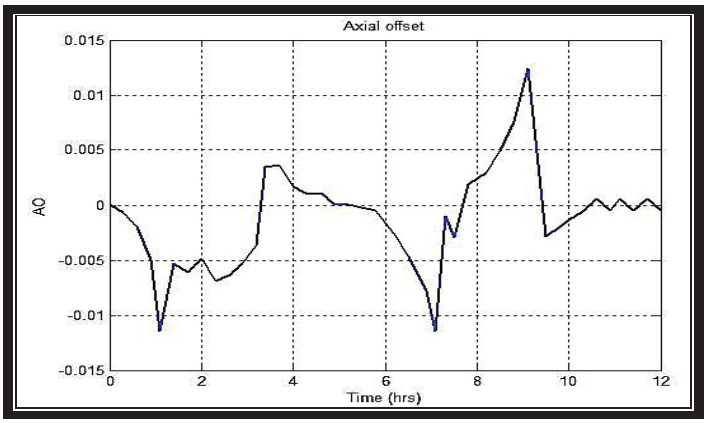

Fig. 10. Variation of axial offset for ramp power changes.

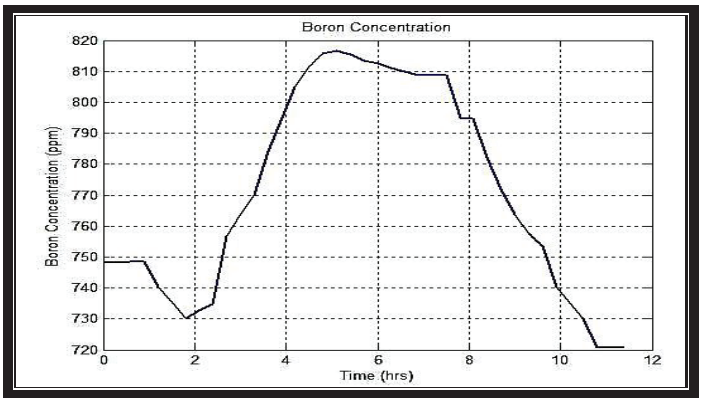

Fig. 11. Variation of boron concentration for ramp power changes.

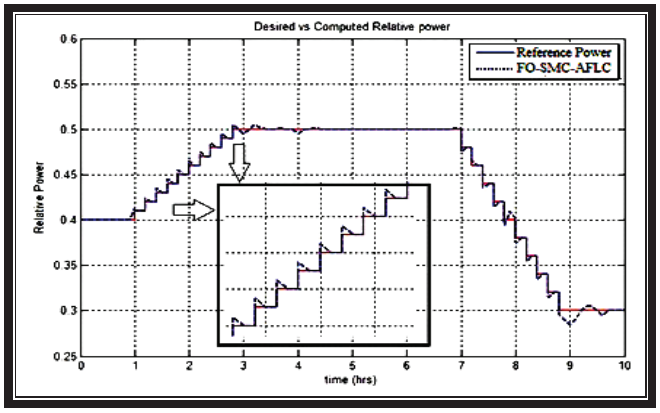

Fig. 12. Comparison of FO-SMC-AFLC and reference reactor powers under step power changes.

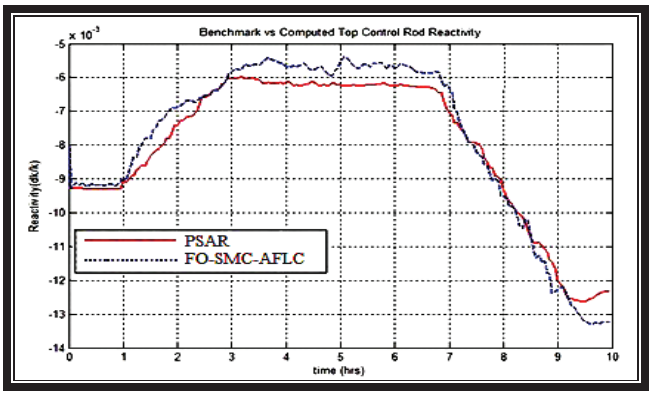

Fig. 13. Performance comparison of top control rod reactivity for step power changes.

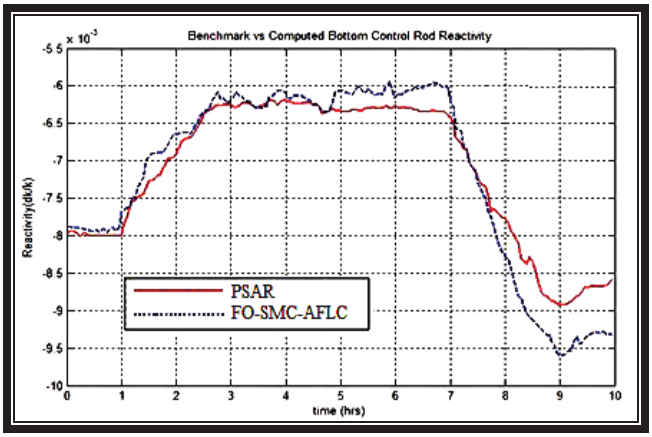

Fig. 14. Performance comparison of bottom control rod reactivity for step power changes.

and shown in Fig. 11. As the reactor power is increased, the boron concentration is diluted but with the passage of time, the xenon concentration is decreased as the reactor power increases. Therefore, to compensate the Xenon dynamics, the boration is accomplished.

3.2.2 Step Transient Simulations

In step power transient, the reactor power is increased from 40% to 50% with 1% power change rate and then the reactor power is decreased from 50% to 30% with 2% power change rate. This is a step change procedure which is adopted in ACP1000 nuclear reactor dynamics. The behaviour of FO-SMC-AFLC based closed loop system is shown in Fig. 12 against the desired step reference signal.

It is very much obvious from Fig. 12 that the relative reactor power tracks well the target step reactor power.

The performance of proposed control system for top and bottom halves of reactor core for step transient is shown in Fig. 13 and Fig. 14, respectively.

The reasons for top and bottom reactivity variations with relative step power are similar as that of ramp power changes.

The performance of the proposed controller in terms of overshoot and settling time for step power changes are well within the designed constraints.

The variations of axial offset and boron concentration are shown in Fig. 15 and Fig. 16 respectively. The performance of the proposed controller in terms of AO band for ramp power changes is well within the designed target band of 0.05. The reasons of boron and Xenon reactivity compensation with step power changes are similar as that of ramp power changes.

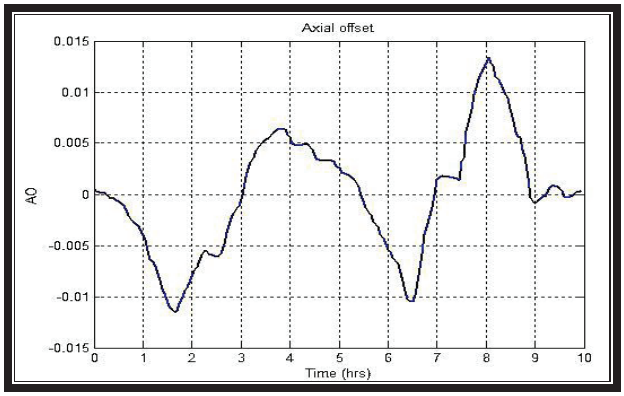

Fig. 15. Variation of axial offset for step power changes.

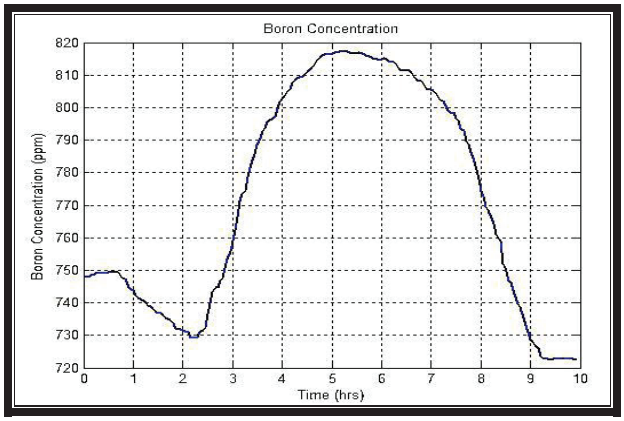

Fig. 16. Variation of boron concentration for step power changes.

4. CONCLUSIONS

wo-point kinetics model of ACP1000 reactor has been developed and reactivity feedbacks have been modeled with special emphasis on G-bank, R-bank RCCA and chemical shim for load following operation. A three input, two output highly nonlinear 26th order MIMO model of ACP1000 reactor dynamics has been developed. MIMO model is decoupled into desired SISO sub-systems. Large reactor core neutronic problems of ACP1000 have been addressed and successfully solved. Two state-of-the-art new controllers have been configured for reactor power compensation, reactivity control and axial power distribution control using most advanced optimized sliding control design algorithms. Both controllers have two SISO sub-controllers for control rod position and boron concentration. Modelling, control design, optimization, simulation and analysis have been accomplished in the MATLAB environment. Transient simulation experiments show that successful realization has been achieved. The extension of research work for other control rod banks with other modes of operations of ACP1000 is straightforward in future.

5. ACKNOWLEDGEMENTS

The support of the Pakistan Atomic Energy Commission, Chashma Centre of Nuclear Training and Computer Development Division of KANUPP is gratefully acknowledged.

10. REFERENCES

1. Preliminary safety report of HPR1000. UKHPR1000GDA Project, Report HPR/GDA/PSR: (2017).
2. T. Xin. Safety approach and safety assessment Hualong HPR1000, IFNEC Report: (2018).
3. L. C. C. Po, and J. M. Link. PCTRAN-3 / U 3-LP. Micro-Simulation Technology: (2018).
4. M. Zirong, and Y. Zenghua. Improvement of M310 PWR-study on the load follow without boron adjustment. *Chinese Journal of Nuclear Science and Engineering* 24 (04): 294-300 (2018).
5. B.Lan, Q. Meng, J. Yang, and Y. Cai. Analysis and application of load change rate algorithm for CPR1000 nuclear power plant, *Journal of Nuclear Power Engineering* 38 (04): 51-55 (2017).
6. C. Wang, J. Gao, and Y. Chai. Design of adaptive fuzzy controllers for a factional order nonlinear MIMO systems with input saturation. *IEEE Access* 8: 1-6 (2020).
7. Y. Deng. Fractional-order fuzzy adaptive controller design for uncertain robotic manipulators. *International Journal Advanced Robotic Systems:* 01-10 (2019).
8. H. Zhang, H. Fang, D. Zhang, X. Luo, and Q. Zou. Adaptive fuzzy sliding mode control for a 3-DOF parallel manipulator with parameters uncertainties. *Complexity:* 01-16 (2020).
9. J. Luo, and H. Liu. Adaptive fractional fuzzy sliding mode control for multivariable nonlinear systems. *Discrete Dynamics in Nature and Society*: 01-11 (2014).
10. Y. Tang, Y. Ying, M. Han, and Q. Lian. Adaptive fuzzy fractional-order sliding mode controller design for antilock braking systems. *Journal of Dynamic Systems, Measurement, and Control* 138 (03): 01-11 (2016).
11. H. Delavari, and R. Jokar. Fractional order adaptive fuzzy terminal sliding mode controller design for a knee joint orthosis. *Amirkabir Journal of Mechanical Engineering* 51 (03): 01-03 (2019).
12. J. Fei, and S. Li. Adaptive fractional high order sliding mode fuzzy control of active power filter. *International Conference on Soft Computing and Intelligent Systems, China*: 576-580 (2018).
13. J. Fei, H. Wang, and D. Cao. Adaptive backstepping fractional fuzzy sliding mode control of active power filter. *Applied Sciences* 09: 01-14 (2019).
14. B. Bourouba, and S. Ladaci. Robust fuzzy adaptive sliding mode stabilization for fractional-order chaos. 32 *Algorithms* 11: 01-17 (2018).
15. N. Ullah, S. Han and M. Khatak. Adaptive fuzzy fractional-order sliding mode controller for a class of dynamical systems with uncertainty. *Transactions of the Institute of Measurement and Control*: 01-15 (2015).
16. G. Li. Modeling and LQG/LTR control for power and axial power difference of load-follow PWR core. *Journal of Annals of Nuclear Energy* 68: 193-203 (2014).
17. B. Puchalski, T. A. Rutkowski, and K. Duzinkiewicz. Fuzzy multi-regional fractional PID controller for pressurized water nuclear reactor. *ISA Transactions* 103: 86-102 (2020).
18. G. Grandi. Simulate-3K models and methodology. *SSP Technical Report* SSP98/13: (2011).